PCCP

RSC Publishing

PERSPECTIVE

Cite this: *Phys. Chem. Chem. Phys.*, 2013, **15**, 10307

Spectral challenges of individual wavelength-scale particles: strong phonons and their distorted lineshapes

Aruna Ravi, Marvin A. Malone, Antriksh Luthra, David Lioi and James V. Coe*

Beyond our own interest in airborne particulate matter, the prediction of extinction and absorption spectra of single particles of mixed composition has wide use in astronomy, geology, atmospheric sciences, and nanotechnology. Single particle spectra present different challenges than traditional spectroscopic approaches. To quantify the amount of a material in a bulk sample (molecules in solution or the gas phase), one might employ the Beer–Lambert law assuming a simple slab-type assay geometry and averaging over orientation, whereas with single particles one might have a specific orientation and require a nonlinear, Mie-like particle theory. The complicating single particle issues include: strong and broad scattering at wavelengths similar to the particle size, phonon lineshape phase shifting, particle shape effects, distortion of transition lineshapes by strong vibrational bands, bi- and trirefringence, crystal orientation effects including dispersion, and composition mixtures. This work uses a combination of three-dimensional finite difference time domain (3D-FDTD) calculations and experimental infrared spectra on single, crystalline quartz particles to illustrate some of the challenges – in particular the distortion of line-shapes by strong phonons that lie within a range of strong scattering. It turns out that many mineral dust components in the inhalable size range have strong phonons. A Mie–Bruggeman model for single particle spectra is presented to isolate the effects of strong phonons on lineshapes which has utility for analysing the spectra of single, mixed-composition particles. This model will ultimately enable the determination of volume fractions of components in single particles that are mixtures of many materials with strong phonons, as are the dust particles breathed into people's lungs.

Received 4th April 2013,
Accepted 14th May 2013

DOI: 10.1039/c3cp51422f

www.rsc.org/pccp

Department of Chemistry and Biochemistry, The Ohio State University, 100 West 18th Avenue, Columbus, Ohio 43210-1173, USA. E-mail: coe.1@osu.edu; Fax: +1 614-292-1685; Tel: +1 614-292-9489

Aruna Ravi

Aruna Ravi received her Master of Science in Electrical Engineering from The University of Texas at Arlington. She is currently pursuing a PhD in Electrical and Computer Engineering at The Ohio State University, Columbus. Her current research interests include plasmonics in the infrared, complex media and metamaterials, computational methods of electromagnetic field theory, especially FDTD techniques.

Marvin Malone

Dr Marvin Malone is a recent PhD graduate in Physical Chemistry from The Ohio State University. Previously he obtained a BS in Chemistry with a minor in Biology from the California State University at Dominguez Hills. He was given the Advancing Science Award in 2011 and 2010 by the National Organization for the Professional Advancement of Black Chemist and Chemical Engineers (NOBCChE) and the Physical Chemistry Teaching Assistant Award in 2009 by The Ohio State University Department of Chemistry.

1. Introduction to single particle spectra

Single particle techniques[1–3] are of interest in many fields of science and include electron microscope and X-ray methods,[4–7] mass spectrometry,[8–10] Raman,[11,12] and infrared (IR) spectroscopy.[13–16] The Coe group records scatter-free infrared (IR) transmission spectra of single particles using plasmonic Ni mesh,[17] *i.e.* by trapping the particles in periodic holes of a thin metal film which suppresses scattering. Experiments have been carried out on polystyrene microspheres,[18] live yeast cells,[19] and previously airborne dust particles.[13,14] This type of single particle IR spectroscopy[13,14] can serve as a quick, quantitative, and non-destructive method that identifies individual particles for further study. Things get interesting when the particles are similar in size to the wavelength of probing light (Fig. 1).

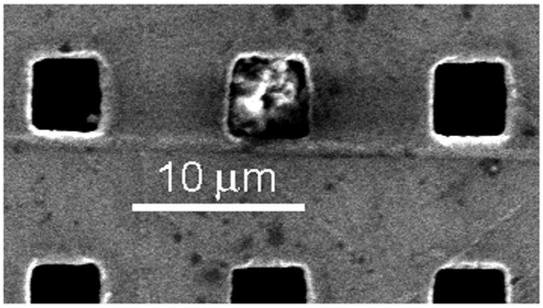

Fig. 1 Scanning electron microscope image of airborne dust particle trapped in a hole of our Ni plasmonic mesh (5 μm square holes, 12.6 μm lattice parameter, 2 μm thick) from which scatter-free absorption spectra are obtained.

While there is much work on scattering,[20,21] this work focuses on vibrational features in spectral regions dominated by scattering. We are particularly interested in quantifying the amount of a particle component by the strength of such vibrational features. In traditional spectroscopic studies with bulk gas phase or solution samples, this is the purview of the Beer–Lambert law,[22,23] *i.e.* the vibrational peak height is linearly proportional to the amount of material. However, things are more complicated with condensed phase particles of wavelength size.[20,21,24] At the least, the spectrum may change with particle orientation and a nonlinear Mie-like theoretical model might be required to analyse vibrational lineshapes.

This work describes three-dimensional finite difference time domain (3D-FDTD) simulations and experimental spectra of individual crystalline quartz particles in order to illustrate some of the difficulties that will occur in ultimately treating dust particle spectra[13,14] which are typically mixtures of multiple mineral components with some organics attached. The 3D-FDTD work is a direct numerical integration of Maxwell's equations[25] and, among other things, the simulations provide a transmission spectrum which needs to be interpreted just like an experiment. Simulations were obtained on slabs and spheres of the same volume in order to assess the applicability of the Beer–Lambert law and to investigate dispersive contributions to lineshape. Then, experimental quartz particle spectra are used to show simple, non-Beer–Lambert behaviour and then more dramatic effects when stronger vibrations are involved. This work ends with a Mie–Bruggeman model that can address many of the spectral challenges discussed in this work. The important effects of

Antriksh Luthra

Antriksh Luthra is a doctoral student in Mechanical Engineering at The Ohio State University, Columbus. He received his Master of Science in Aerospace Engineering from The University of Texas at Arlington. His current research focuses on infrared spectroscopy, plasmonics and applications, scattering and absorption of light by particulate matter, and fabrication of plasmonic bi-gratings. He is a member of the Tau Beta Pi National Engineering Honor Society and a recipient of the Robert H. Edgerley Environmental Toxicology Travel Award for 2013.

David Lioi

David Lioi is an undergraduate researcher at The Ohio State University majoring both in chemistry and physics. His interests include condensed matter, metamaterials, plasmonics and solar cell technology.

James V. Coe

Professor James V. Coe, Department of Chemistry and Biochemistry, The Ohio State University. He received his BA in chemistry from Swarthmore College, a PhD in physical chemistry from The Johns Hopkins University (supervised by Kit H. Bowen), and did a postdoc at the University of California at Berkeley (supervised by Richard J. Saykally). He is a fellow of the American Physical Society. Current research involves finding applications of plasmonics in chemistry.

particle shape[21,26] and phonon dispersion are not treated in this work in order to keep the scope manageable. There are a number of fundamental questions of interest: how does scattering affect strong vibrational lineshapes? When is the Beer–Lambert law valid? How do you treat mixtures of components in a particle?

2. Particle vibrations, theoretical models, and the phase problem

The position, intensity, and width of vibrational peaks are readily measured quantities that are usefully encoded in many models. Both 3D-FDTD simulations and Mie theory require the complex index of refraction (m) of the subject particle which varies with wavelength. Vibrational transitions are often added as damped harmonic oscillators (classical dispersion theory) to the permittivity (ε) of the dielectric material, whose square root is the complex index of refraction (m):

$$m^* = \sqrt{\varepsilon} = \sqrt{\varepsilon_0 + \sum_j \frac{A_j \tilde{\nu}_{0,j}{}^2}{\tilde{\nu}_{0,j}{}^2 - \tilde{\nu}^2 - i2\Gamma_j\tilde{\nu}}}, \tag{1}$$

where j is an index over the vibrations, ε_0 is the constant complex dielectric, A_j is the unitless strength of each vibration (*i.e.* in dielectric units), $\tilde{\nu}_{0,j}$ is the position of each vibration in wavenumbers, and $2\Gamma_j$ is the full-width-at-half-max (FWHM) of the feature in wavenumbers, *i.e.* Γ_j is the half-width-at-half-max (HWHM). An illustration using Mie theory is given in Fig. 2 which shows the broad scattering background exhibited by a 5 μm diameter spherical particle with (dashed trace) and without (solid trace) a vibration (parameters are given in the figure caption). The extinction spectrum was calculated using Bohren and Huffman's[21] subroutine (appendix of 1987 edition gives Fortran code, other languages are available at http://code.google.com/p/scatterlib/wiki). Note several features: a broad scattering feature with a maximum near the size of the particle, an intensity maximum that is four times the physical cross section of the particle, wiggles which correspond to constructive and destructive interference with the spherical shape, and a vibrational feature with a large dispersive contribution (it looks more like a derivative than a Lorentzian). The scattering maximum is ~5 times as intense as the vibrational feature which itself has a cross section similar to that of the particle. This illustrates a situation dominated by scattering with a severe change in the vibrational lineshape which can be largely attributed to a phase shift. The phase shift (φ), intensity (S/Γ), position ($\tilde{\nu}_0$), and HWHM (Γ) can be determined by fitting the difference in the two traces (with and without the vibration) to the following absorption–dispersion lineshape[27]

$$E(\tilde{\nu}) = \frac{\frac{S}{\Gamma}\left[\cos\varphi - \left(\frac{\tilde{\nu}-\tilde{\nu}_0}{\Gamma}\right)\sin\varphi\right]}{1 + \left(\frac{\tilde{\nu}-\tilde{\nu}_0}{\Gamma}\right)^2} + C \tag{2}$$

where C is a constant added for better fits with nonflat baselines. A nonlinear least squares fit of the phonon lineshape produced $S/\Gamma = 2.65 \pm 0.05 \times 10^{-7}$ cm^2, $\tilde{\nu}_0 = 3204.8 \pm 0.6$ cm^{-1}, $\Gamma = 22.0 \pm 0.6$ cm^{-1}, and $\varphi = 271 \pm 4°$. Understand that this transition was chosen because its intensity (in cross section units) is a bit larger than the physical cross section of the particle (1.96×10^{-7} cm^2). While the transition is reasonably located by the fit, the fitted width (obtained as HWHM) is more than four times the input value. So, the transition is extensively phase shifted and broader than expected. Eqn (2) accounts for phase effects: if the phase (φ) is zero, then $\sin\varphi = 0$, and one obtains the normal Lorentzian lineshape associated with absorption. When φ is 90°, then $\cos\varphi = 0$, and one obtains a pure dispersive lineshape that goes up and down. If the phase is determined, an intensity can be extracted even when the lineshape has both absorbance and dispersion contributions. In other words, one can interpret the signal as a Lorentzian lineshape even though it was measured with dispersive contributions. However, in the Fig. 2 example, the phonon linewidth is increasing because the particle size is comparable to the probing wavelength.

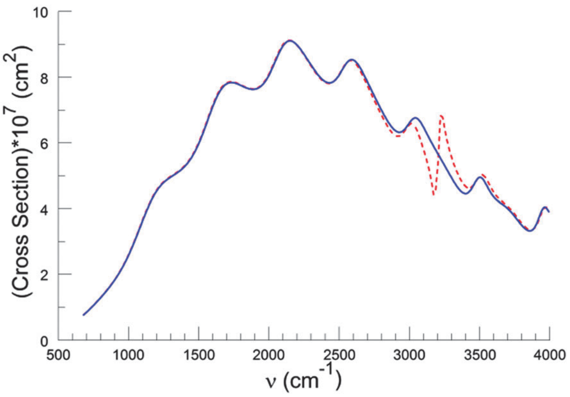

Fig. 2 Extinction spectrum (cross section) of a 5 μm diameter spherical particle with a refractive index of 1.60 as calculated by Mie theory without a single vibration (solid trace) and with a vibration (dashed trace). The eqn (1) parameters for the vibration were $A = 0.005$, $\tilde{\nu}_0 = 3200$ cm^{-1}, and $\Gamma = 5$ cm^{-1} and the physical cross section of the particle is 1.96×10^{-7} cm^2.

3. 3D-FDTD simulations of slabs and spheres: testing the Beer–Lambert law

To better illustrate the single particle issues, spectral simulations were performed on a sequence of slabs and spheres of equal volumes to each of which a single vibrational feature was added. The spheres were chosen so that their diameters tune through the phonon transition wavelength region. The software was "FDTD Solutions 8.0.4" from Lumerical, Inc. (Vancouver, BC; www.lumerical.com). Initially, the simulation regions were 10 μm × 10 μm × 80 μm for both the slabs and spheres (as shown in Fig. 3). Since the spheres do not share the symmetry of the cell, a larger cell of 20 μm × 20 μm × 80 μm was employed for the spheres (Fig. 4) in order to reduce possible boundary effects. Unlike the slabs, small changes in a spherical particle's simulation cell can be expected to change spectral lineshape with our detector geometry. Simulation parameters included auto non-uniform

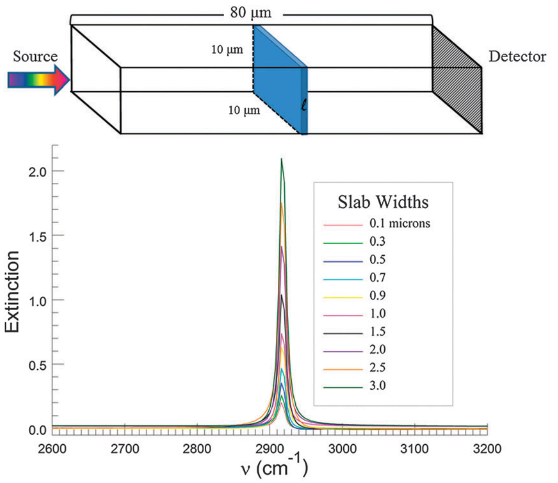

Fig. 3 Plot of the extinction without vibration subtracted from extinction with vibration (in units of 10^{-7} cm^2) for slab pathlengths, ℓ, of 0.1, 0.3, 0.5, 0.7, 0.9, 1.0, 1.5, 2.0, 2.5, and 3.0 μm. Results calculated using 3D-FDTD simulations. A schematic of the simulation is provided at top.

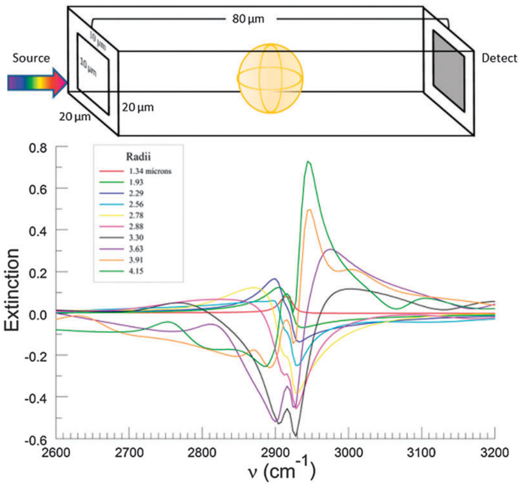

Fig. 4 Plot of the extinction without vibration subtracted from extinction with vibration (in units of 10^{-7} cm^2) for sphere radii, of 1.34, 1.93, 2.29, 2.56, 2.78, 2.88, 3.30, 3.63, 3.91, and 4.15 μm. Results calculated using 3D-FDTD simulations. Schematic of the simulation is provided at top.

Table 1 Slab fit parameters according to eqn (2) of the spectra in Fig. 3. The dielectric input parameters [$A = 0.005$, HWHM = 5.0 cm^{-1}, and $\nu_0 = 2917.0$ cm^{-1}] were accurately recovered

Vol. (μm^3)	S/Γ (cm)	φ (rad.)	Γ (cm^{-1})	ν_0 (cm^{-1})
10.0	0.2039(6)	0.231(3)	5.64(3)	2917.18(3)
30.0	0.2640(5)	0.254(2)	5.57(2)	2917.58(2)
50.0	0.3730(4)	0.263(1)	5.31(1)	2917.96(1)
70.0	0.511(3)	0.108(3)	4.86(2)	2917.82(2)
90.0	0.694(2)	−0.023(3)	4.97(2)	2917.44(2)
100.0	0.781(2)	−0.031(3)	5.17(2)	2917.38(2)
150.0	1.131(1)	0.109(4)	5.24(3)	2917.92(2)
200.0	1.535(1)	−0.038(4)	5.13(3)	2917.43(3)
250.0	1.908(8)	0.074(5)	5.33(3)	2917.84(2)
300.0	2.313(21)	−0.024(5)	4.98(4)	2917.55(4)

Table 2 Sphere fit parameters according to eqn (2) of the spectra in Fig. 4

Vol. (μm^3)	S/Γ (cm)	φ (rad.)	Γ (cm^{-1})	ν_0 (cm^{-1})
10.0	0.0864(1)	0.213(15)	9.7(2)	2916.0(2)
30.0	0.192(3)	1.217(16)	15.5(3)	2917.7(4)
50.0	0.277(7)	1.42(3)	16.9(8)	2915.3(8)
70.0	0.289(9)	2.20(4)	17.0(9)	2920.7(9)
90.0	0.463(24)	2.18(4)	24.7(12)	2915.9(12)
100.0	0.489(19)	2.64(6)	24.8(17)	2918.9(17)
150.0	0.70(3)	3.75(7)	28.0(8)	2930(4)
200.0	0.78(3)	4.47(8)	28.5(21)	2936(4)
250.0	0.62(4)	5.03(9)	28.3(31)	2932.7(28)
300.0	0.85(4)	5.51(7)	20.9(18)	2938.2(17)

meshing and all absorbing, perfectly matched layer (PML), boundary conditions. The source was a plane wave propagating parallel to the z-axis (left to right) with dimensions of 10 μm × 10 μm and it was placed −40 μm from the slab which was centered. The detector was the same size and positioned at the end of the simulation cell. The extinction spectrum without the vibration was subtracted from the identical simulation with the vibration ($\varepsilon_0 = 2.3 + i0.0$, $A = 0.005$, $\tilde{\nu}_0 = 2917.0$ cm^{-1}, $\Gamma = 5.0$ cm^{-1}) in each trace in Fig. 3 and 4. The slabs of Fig. 3 are all 10 μm × 10 μm having thicknesses of 0.10, 0.30, 0.50, 0.90, 1.00, 1.50, 2.00, 2.50, and 3.00 μm. Each sphere of Fig. 4 has the same volume as a corresponding slab in Fig. 3. The sphere radii are 1.34, 2.29, 2.56, 2.78, 2.88, 3.30, 3.63, 3.91, and 4.51 μm. All of the lineshapes in Fig. 3 and 4 were fit to eqn (2) yielding the data in Tables 1 and 2.

The fits and residuals of similar calculations are available in Marvin Malone's PhD thesis.[28] The slab lineshapes follow a pattern related to the Beer–Lambert law where absorbance (A, is the negative of the common log of the ratio of transmittance with and without sample)

$$A = -\log(t/t_0) = \bar{\varepsilon}\ell C, \tag{3}$$

is related to the molar extinction coefficient of the sample ($\bar{\varepsilon}$, which changes with wavelength), the path length of light through the solution (ℓ), and the molar concentration of the solute (C). For purposes of comparing to particles, the slab line strengths will also be proportional to slab volume within the simulation cell. Scattering is ignored, *i.e.* the phase (ϕ) is assumed to be zero (absorbance dominated). Linewidths are assumed to be constant and line strengths increase with the thickness (or volume) of the slab. These are the predominant features of the slab results of Fig. 3, although subtle hints of scattering are evident upon close examination of the tables. The spheres of Fig. 4 show dramatic changes in lineshape and phase [φ of eqn (2)] and they have mixtures of absorbance and dispersion contributions. The question is whether the spheres, after correcting for phase, are still following a Beer–Lambert-like trend. A plot of the intensity (S/Γ) *vs.* volume is given in Fig. 5. The spheres diverge significantly from the Beer–Lambert law trend at larger volumes. In fact, the phased Lorentzian lineshape model of eqn (2) becomes inadequate for spheres whose diameters are similar to the strong phonon transition wavelength.

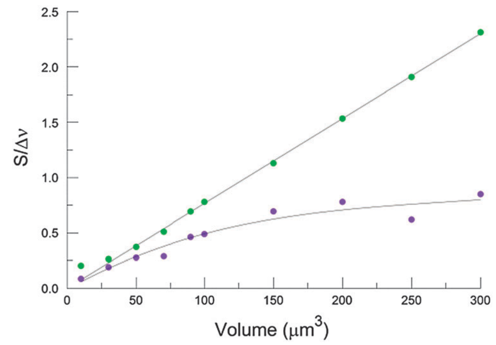

Fig. 5 Plot of the intensity, S/Γ *versus* volume for the slab (green circles) and sphere (purple circles) as determined by fitting the lineshapes in Fig. 3 and 4. The lines are 1st and 3rd order polynomial fits to guide the eye.

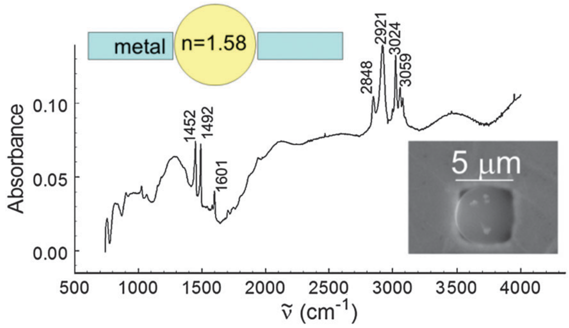

Fig. 7 The average absorption spectrum of 19 single and isolated, 5 μm polystyrene microspheres in mesh holes. The bottom inset is a SEM image of a polystyrene microsphere in a mesh hole. The top inset is a cross section view of the particle in the mesh hole.

4. The phase problem is reduced by trapping particles in plasmonic metal hole arrays

Metal films with arrays of tiny holes (mesh) display enhanced zero-order transmission spectra, that are mediated by surface plasmon polaritons.[17,29,30] This area of research took flight in 1998 when Ebbesen and co-workers fabricated square arrays of nano-scale cylindrical holes in metallic films and measured unexpectedly high resonant transmissions in the visible and near IR regions.[31] It turns out that the scattering properties of wavelength-scale particles are dramatically affected by placing the particle in a hole of the plasmonic mesh.[18] In oversimplified terms, the infrared light is trapped at the surface of the metal and the particle in a subwavelength mesh hole is exposed to light in a manner more like an attenuated total reflection probe (from all hole sides) rather than as an isolated particle under direct radiation.

Latex microspheres of 5.0 μm diameter can be expected to show extensive scattering effects in the mid IR region as illustrated by the extinction spectrum of Fig. 6.[18] The spectrum is actually an average of the spectra of 16 different particles of a fairly monodisperse sample. The spectrum is large and broad – dominated by scattering – as the particle size is similar to the probing wavelength (just like Fig. 2). In the normal Beer–Lambert regime, absorption is dominant and scattering has a minimal contribution and is therefore ignored. However, a single, wavelength-scale particle has much more scattering than absorption, so scattering cannot be ignored. In fact, the spectrum in Fig. 6 is well accounted for with Mie theory. Consider the vibrational transitions: they are roughly 10 times weaker than the scattering and they have large phase shifts (lineshape phase distortions) relative to simple absorption spectra.

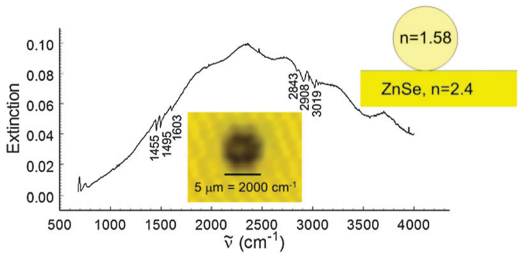

Fig. 6 The average extinction spectrum of sixteen different, 5 μm polystyrene (n = 1.58) microspheres on a ZnSe (n = 2.4) infrared window. The bottom inset is an optical image of a polystyrene microsphere on top of ZnSe taken with the Perkin Elmer Spotlight 300 infrared imaging microscope. The top inset is a schematic side view.

When 5.0 μm microparticles of the same monodisperse sample are placed into plasmonic Ni mesh holes (12.6 μm square lattice, 5.5 μm square holes, 2 μm thick), the dominant effects of scattering are remarkably reduced as shown in Fig. 7. The vibrations are now the largest features and the phase [φ of eqn (2)] is close to zero, a value like pure absorption. Both spectra in Fig. 6 and 7 are averages over many particles of the same sample and were recorded under the same conditions (18.75 μm by 18.75 μm microscope window, 512 scans, 4 cm^{-1} resolution). Matsumoto and coworkers[32] have shown that plasmonic field enhancements are observable if the holes become small enough (~2 μm) relative to the lattice parameter (12.7 μm). The hole widths of this work (~5 μm) are well above this threshold and are therefore useful for quantitatively characterizing the amounts of materials. While the plasmonic mesh certainly facilitates analysis, it became apparent that a number of more subtle and interesting spectral problems become evident as discussed below.

5. Single quartz particle spectra with plasmonic mesh: strong vibrations

Quartz is one of the most prevalent mineral components in airborne particulate matter,[14,33–37] *i.e.* people routinely breathe it into their lungs. Breathing in too much quartz is the cause of silicosis,[38] so it is important to know the distribution of quartz in ordinary airborne particulate matter as an indication of tolerable levels. Spectra of pure crystalline quartz were recorded as a calibration for the quartz in our laboratory air.[14] IR "scatter-free" spectra were recorded of 15 different, single α-quartz particles in plasmonic metal mesh holes, as shown in Fig. 8. These spectra are a bit disappointing as calibration because each spectrum is unique due to variation in size (range of ~3–5 μm diameters) and orientation. Quartz phonons are

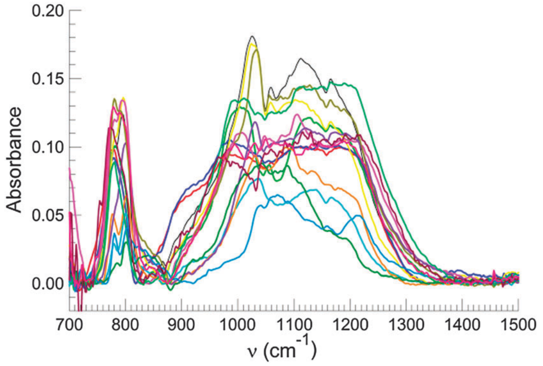

Fig. 8 IR scatter-free spectra of 15 different, single α-quartz particles showing variations with orientation and size.

divided into two groups (ordinary and extraordinary) due to birefringence. The groups have transition moments perpendicular to each other. There are two notable effects to be extracted from these spectra: (1) non-Beer–Lambert behaviour of the ''normal'' looking pair of peaks at 777 and 799 cm^{-1} and (2) intense lineshape broadening and distortion of the most intense asymmetric SiO_4 stretching vibrations at 1072 and 1080 cm^{-1}.

The band at 777 cm^{-1} is extraordinary and the band at 799 cm^{-1} is ordinary, *i.e.* a crystal orientation that is good for detecting one will be bad for the other and *vice versa*. Note that there exist *ab initio* calculations on α-quartz which can be very helpful[39] for phonon spectra. The intensities of these bands were originally measured in reflection by Spitzer and Kleinman[40] [one of the first applications of classical dispersion theory, *i.e.* eqn (1)]. These bands are ∼6 times weaker [by the *A* parameter of eqn (1)] than the strongest bands according to Spitzer's work and ∼9–10 times weaker according to an harmonic *ab initio* calculation.[39] These two peaks in all 15 individual spectra were fit to Gaussian lineshapes with a nonlinear least squares fitting routine and a representative fit is shown in Fig. 9. A plot of the fitted peak widths *vs.* peak intensity is presented in Fig. 10.

If these peaks of medium strength were obeying the Beer–Lambert relation, then the peak widths would remain constant, but there is clearly a trend that more intense peaks are also broader. This non-Beer–Lambert behaviour is problematic enough (a factor of two increase in band width and a less than linear rise in intensity with an increase in volume), but it is a subtle effect when compared to the behaviour of a stronger transition. Basically, these lineshape effects are manifest when the cross section attributed to the vibration (as calculated with Mie theory) becomes comparable to the physical cross section of the particle.

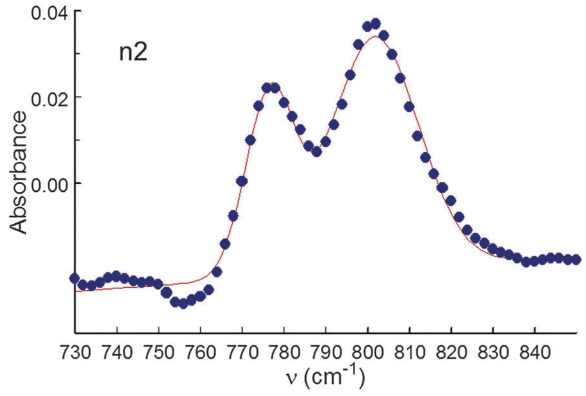

Fig. 9 Nonlinear least square fits of the extraordinary and ordinary peaks at 777 and 799 cm^{-1} which will be used to test the Beer–Lambert behaviour.

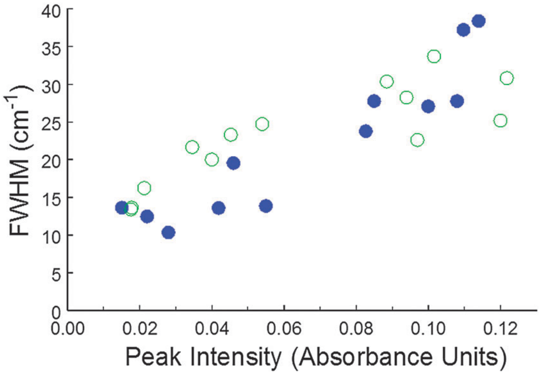

Fig. 10 Nonlinear least square fitted values of peak width (full-width-at-half-maximum, FWHM) *vs.* peak intensity for 15 α-quartz particles. Beer–Lambert behaviour would give rise to a flat trend with constant width. Characteristic quartz bands at 777 cm^{-1} (A_2 symmetry, extraordinary, blue) and 799 cm^{-1} (*E* symmetry, ordinary, green) show systematic increases in band width with increases in absorption, *i.e.* non-Beer–Lambert behavior.

The lineshape effects are much more dramatic for the peaks at 1072 (*E* symmetry, ordinary) or 1080 cm^{-1} (A_2 symmetry, extraordinary) which are the strongest phonons for quartz[40] [A = 0.67 of eqn (1) by reflection[40] and 3300 or 1800 km mol^{-1} linestrength by *ab initio*[39]]. As is evident in Fig. 8, the bands in this region extend over a range of 400 cm^{-1}, they are curiously flattened, not six times stronger than the bands at 777 and 799 cm^{-1}, and there appear to be more peaks than there are fundamentals. These types of lineshape distortions can be found with simple Mie theory if one greatly increases the value of *A* as shown in Fig. 11. Clearly there is intensity capping, widespread broadening rather than an intensity increase, and there is lineshape distortion with multiple shifted peaks. One might say that as the integrated band intensity increases, the peak widens instead of growing taller. Apparently, a band's height in cross section units will not greatly exceed the particle's physical cross section. These dramatic changes can be very different than spectra observed with bulk samples. It turns out that many common minerals (quartz, carbonates, clays, and gypsum) that are found in airborne particulate matter have phonons that are strong enough to show these ''particle saturation'' effects. While this is certainly a disadvantage for quantifying the volume fractions of particle components, perhaps there are also new research opportunities here. The ability to tailor particle size on the wavelength scale apparently affords the ability to dramatically alter the lineshape. Although Fig. 11 serves as a nice illustration of particle lineshape saturation effects, mineral transition strengths are known, *i.e.* they are not a variable. In the following section, we will develop a Mie–Bruggeman model that obtains such effects with a constant value of phonon intensity, *A*.

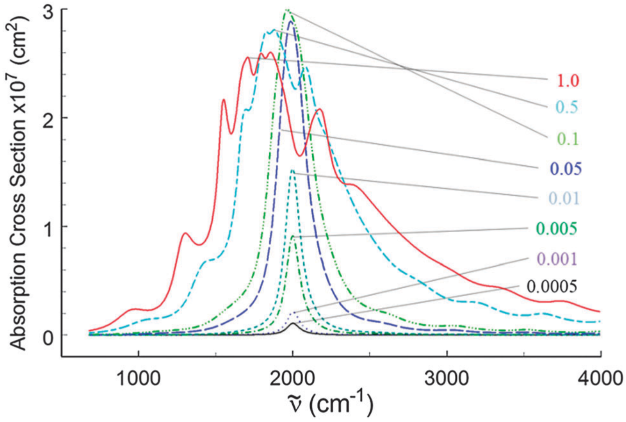

Fig. 11 Lineshape distortion with a strong phonon as calculated with Mie theory. Plot of the absorption cross section of a 2.5 μm radius particle (ε = 2.56 + i0.00) with a single phonon transition of $\tilde{\nu}_0$ = 2000 cm^{-1} and Γ = 100 cm^{-1}. The strength, A, was increased from 0.0005 to 1.0 in a number of steps. There is a single peak at low intensities, however one obtains multiple maxima at intensities above A = 0.1.

6. Mie–Bruggeman model solves some of the problems

To address the issues of birefringence, orientation, strong phonons, and mixtures of different materials, a combination of Mie theory[20,21] with Bruggeman's effective medium theory[41,42] has been developed. The basic idea of Bruggeman effective medium theory is to combine the pure dielectric function of the components of a mixture to obtain an effective dielectric function of the mixture as illustrated in Fig. 12. While it is straightforward to apply this to mixtures, one can also consider different symmetry groups of phonons to be different materials enabling the model to treat birefringence. An effective index of refraction for a mixture of materials within a particle can, in turn, be used with Mie theory to calculate the spectrum of the particle of mixed composition. The grand equation of Bruggeman's effective medium theory is

$$\sum_i f_i\left(\frac{\varepsilon_i - \varepsilon_{\mathrm{eff}}}{\varepsilon_i + 2\varepsilon_{\mathrm{eff}}}\right) = 0, \qquad (4)$$

where i is an index over the components, f_i is the volume fraction of the ith component, ε_i is the pure dielectric constant for each component, and $\varepsilon_{\mathrm{eff}}$ is the effective dielectric of the mixed particle. Using an initial guess of the volume fractions and the known dielectrics of pure components, $\varepsilon_{\mathrm{eff},0} = \Sigma_i f_i \varepsilon_i$, an iterative function has been derived which refines the effective dielectric function based on the previous iteration

$$\varepsilon_{\mathrm{eff},k} = \left[\sum_i\left(\frac{f_i\varepsilon_i}{\varepsilon_i + 2\varepsilon_{\mathrm{eff},k-1}}\right)\right]\Bigg/\left[\sum_i\left(\frac{f_i}{\varepsilon_i + 2\varepsilon_{\mathrm{eff},k-1}}\right)\right], \qquad (5)$$

where k is the number of iterations. We find about 10 iterations sufficient for convergence. This effective dielectric can be used with Mie theory to predict extinction, scattering, or absorption spectra of mixed particles.

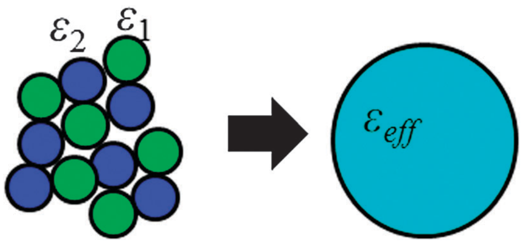

Fig. 12 Illustration of Bruggeman's effective medium theory for two components of different dielectric ε_1 and ε_2.

Recall from Section 5 on the experimental spectra of α-quartz particles that there were two big issues: (1) non-Beer–Lambert behaviour of the "normal" looking pair of peaks at 777 and 799 cm^{-1} and (2) intense lineshape broadening and distortion of the most intense asymmetric SiO_4 stretching vibrations at 1072 and/or 1080 cm^{-1}. By treating the ordinary phonon transitions of E symmetry (including the 799 cm^{-1} transition) as one material [with the dielectric parameters: ε = 2.356 + i0.000, A = 0.11 (from Spitzer and Kleinman[40]), $\tilde{\nu}_0$ = 797 cm^{-1}, and Γ = 20 cm^{-1}] and by treating the extraordinary transitions of A_2 symmetry (including the 777 cm^{-1} transition) as another material [with the dielectric parameters ε = 2.383 + i0.000, A = 0.10 (from Spitzer and Kleinman[40]), $\tilde{\nu}_0$ = 778 cm^{-1}, and Γ = 20 cm^{-1}], the two can be combined with the Mie–Bruggeman model as shown in Fig. 13 to predict infrared spectra. In the model one varies the volume fraction of each component, but as applied in this case, one is actually changing the component of the transition moment excited as the particle's orientation is changed. To be quantitative, one must of course consider the conditions under which the spectra were acquired (in our case an IR microscope using unpolarized light with averaging over a range of angles tilted from the microscope axis). Rather than getting distracted about such details, note that there certainly exists a range of orientations where the contributions of each transition moment are equal as shown in Fig. 13.

Unlike experiments (where you cannot turn off a phonon), the Mie–Bruggeman model allows one to examine the subtle lineshape effects of just one of these transitions, *i.e.* the extraordinary band

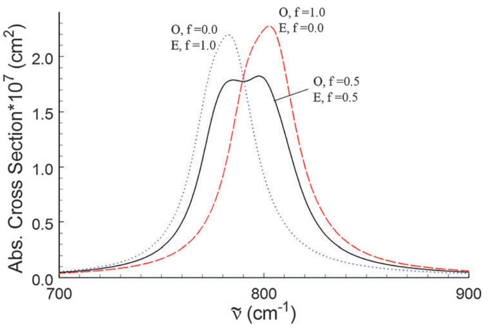

Fig. 13 Absorption cross section of a 4.0 μm diameter spherical particle calculated using a Mie–Bruggeman model where the ordinary (O) and extraordinary (E) contributions of quartz are taken as two separate components. In the model, f is the volume fraction, but for this application with birefringent materials, f is a parameter that changes with orientation. When f = 0, the transition moment is parallel to the incoming light. The orientations when f = 0.5 have components of each transition moment that are equal.

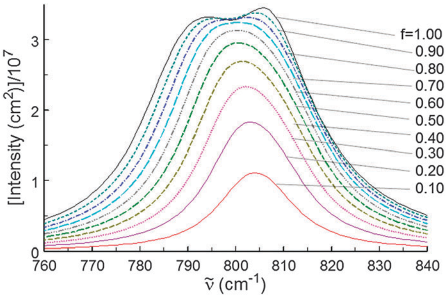

Fig. 14 Absorption cross section of a 5.0 μm diameter spherical particle calculated using a Mie–Bruggeman model where the ordinary and extraordinary contributions of quartz are taken as two separate components. Only the ordinary contribution is shown [A = 0.10 (from Spitzer and Kleinman[40]), $\tilde{\nu}_0$ = 799 cm^{-1}, and Γ = 15 cm^{-1}], *i.e.* the intensity of the extraordinary band has been artificially set to zero. The f parameter is the volume fraction, but for this application with birefringent materials, f changes with orientation. Note how dramatically the linewidth changes with orientation.

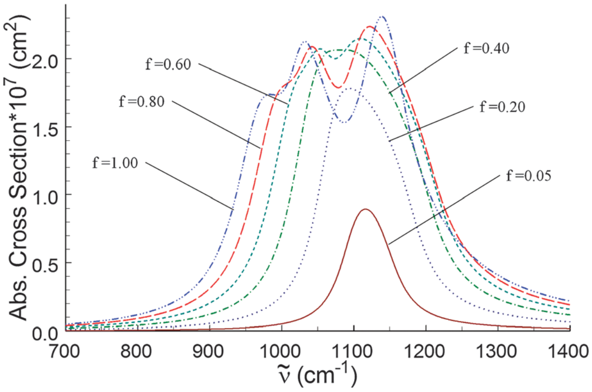

Fig. 15 Absorption cross section of a 4.0 μm diameter spherical particle calculated using Mie–Bruggeman theory taking the ordinary and extraordinary groups as separate materials. The transition shown is the ordinary with A = 0.67, $\tilde{\nu}_0$ = 1072 cm^{-1}, and Γ = 50 cm^{-1}.

strength was set to zero. Fig. 14 shows only the ordinary transition (799 cm^{-1}) as orientation is changed using a fixed linestrength (A = 0.10, given by Spitzer and Kleinman[40] for this transition). These conditions produce a line whose width can more than double with orientation. Note that the Mie–Bruggeman model is providing a quantitative explanation of the experimental quartz data presented earlier in Fig. 10.

While Mie theory shows severe lineshape distortion (Fig. 11), it does so by increasing the linestrength parameter, A. In actual materials, the linestrength is a constant, so it is noteworthy that the Mie–Bruggeman model obtains the observed lineshape distortions with a value of A fixed by experiment.

Clearly, the Mie–Bruggeman model embodies the observed line broadening effects which are no doubt made dramatic by particles of this specific size. Note how the strongest orientation actually produces a doubling which we have not observed experimentally with this transition. However, this suggests severe effects for phonons with even stronger transitions and many common minerals (quartz, carbonates, clays, and gypsum) in airborne dust have strong phonons.

The Mie–Bruggeman model has also been used to model severe phonon lineshape distortions with a stronger transition and changes of orientation. Quartz has two strong phonon transitions at 1072 cm^{-1} (E, ordinary) and 1080 cm^{-1} (A_2, extraordinary) which were originally measured in reflection with linestrengths[40] of A = 0.65. Examining only the ordinary transition [with the dielectric parameters: $\varepsilon = 2.356 + i0.000$, A = 0.67 (from Spitzer and Kleinman[40]), $\tilde{\nu}_0$ = 1072 cm^{-1}, and Γ = 50 cm^{-1}] one obtains severe lineshape distortion. Only at orientations, such as f = 0.05, where this transition is poorly aligned for excitation, will it have a "normal" Lorentzian appearance. All lineshapes with $f > 0.5$ have multiple maxima and shoulders. Considering that there will be similar behaviour for the extraordinary component (not shown), it should be apparent that this transition can be quite complicated.

Going back to the experimental spectra of the 15 α-quartz particles in Fig. 8, we now begin to understand why the bands can extend over a 400 cm^{-1} region. The Mie–Bruggeman model of Fig. 15 shows a single band extending over a broad and similar region. Just as the experimental bands are curiously flattened, the Mie–Bruggeman model of Fig. 15 shows that the peak stops getting taller at orientations corresponding to $f \sim 0.4$ and instead gets wider. Even though the transitions at 1072 and 1080 cm^{-1} are 6–10 times stronger than the transitions at 777 and 799 cm^{-1}, they stop getting taller due to this particle saturation effect and have similar height to the weaker transitions. At many orientations ($f > 0.5$ in Fig. 15), the wide band shows multiple maxima and shoulders. The experimental spectra are even more dramatic in the 900–1300 cm^{-1} region because both the ordinary and extraordinary bands can exhibit severe and overlapped lineshape distortion. Basically, such problems will be encountered whenever the phonon (or vibrational) cross section approaches or exceeds the geometric cross section of the particle. The Mie–Bruggeman model is a good starting point for understanding the strange lineshape effects that can occur when the probing wavelength is comparable to size of the particle.

7. Summary and outlook

Single particle spectral studies now extend from microparticles to individual molecules.[43,44] While it is apparent that researchers must address an entirely different set of issues (like blinking) when studying small numbers of molecules, we were not expecting to find many surprises at the micron scale. Clearly wavelength-scale particles have their own unique set of challenges. At small sizes relative to the wavelength, particles exhibit Beer–Lambert-like behavior. As the particle size increases to about the wavelength, this behavior begins to diverge from Beer–Lambert as shown with our FDTD simulations. The spectral lineshapes of wavelength scale particles can be distorted by phase, saturation, and orientation as seen in both the FDTD simulations and experimental quartz particle spectra. The effects of phase shift on lineshapes of spectra of single particles of wavelength scale are well known. With a little analysis, the phase can be determined and linestrengths extracted. On the other hand, our plasmonic mesh physically took care of the vibrational phase effect problem. However, it enabled us to face a number of other challenges: variation in band intensity with orientation, the widening of lines with orientation, nonlinear band heights with particle volume, and severely distorted lineshapes for strong bands. The Mie–Bruggeman model gives us a simple, quantitative handle on such effects.

We have come to this perspective in order to better understand the single particle IR spectra of individual air borne dust particles. The concentration of such particulate matter is well-known to be correlated with public health. The Coe group has been successful at chemically evaluating individual dust particles in the 3–5 μm size regime (among the largest that get into people's lungs), and has created a library of scatter-free IR spectra of 63 airborne, ~4 μm diameter, dust particles, collected by pumping laboratory air through plasmonic metal mesh.[14] The next step is to use the Mie–Bruggeman model to determine the volume fractions of the various components of airborne particulate matter mixtures.

Acknowledgements

We thank the National Science Foundation for support of this work under Grant No. CHE-1213293.

References

1 P. I. Raynal, E. Quirico, J. Borg, D. Deboffle, P. Dumas, L. d'Hendecourt, J. P. Bibring and Y. Langevin, *Planet. Space Sci.*, 2000, **48**, 1329–1339.

2 U. Kirchner, R. Vogt, C. Natzeck and J. Goschnick, *J. Aerosol Sci.*, 2003, **34**, 1323–1346.

3 S. Nie and S. R. Emory, *Science*, 1997, **275**, 1102.

4 G. J. Flynn, L. P. Keller, C. Jacobsen and S. Wirick, *Meteorit. Planet. Sci.*, 1999, **34**, A36.

5 G. J. Flynn, L. P. Keller, S. Wirick, C. Jacobsen and S. R. Sutton, *J. Phys. IV*, 2003, **104**, 367–372.

6 S. A. E. Johansso, *Analyst*, 1992, **117**, 259.

7 A. Laskin, J. P. Cowin and M. J. Iedema, *J. Electron Spectrosc. Relat. Phenom.*, 2006, **150**, 260–274.

8 D. M. Murphy and D. S. Thomson, *Aerosol Sci. Technol.*, 1995, **22**, 237–249.

9 S. H. Lee, D. M. Murphy, D. S. Thomson and A. M. Middlebrook, *J. Geophys. Res.: Atmos.*, 2002, **107**, AAC 1.

10 D. M. Murphy, D. J. Cziczo, K. D. Froyd, P. K. Hudson, B. M. Matthew, A. M. Middlebrook, R. E. Peltier, A. Sullivan, D. S. Thomson and R. J. Weber, *J. Geophys. Res.: Atmos.*, 2006, **111**, D23S32.

11 B. Wopenka, *Earth Planet. Sci. Lett.*, 1988, **88**, 221–231.

12 J. F. Widmann, C. L. Aardahl and E. J. Davis, *TrAC, Trends Anal. Chem.*, 1998, **17**, 339.

13 M. A. Malone, M. McCormack and J. V. Coe, *J. Phys. Chem. Lett.*, 2012, **20123**, 720–724.

14 K. E. Cilwa, M. McCormack, M. Lew, C. Robitaille, L. Corwin, M. A. Malone and J. V. Coe, *J. Phys. Chem. C*, 2011, **115**, 16910–16919.

15 H.-J. Jung, M. A. Malek, J. Ryu, B. Kim, Y.-C. Song, H. Kim and C.-U. Ro, *Anal. Chem.*, 2010, **82**, 6193–6202.

16 S. Maskey, H. Geng, Y.-C. Song, H. Hwang, Y.-J. Yoon, K.-H. Ahn and C.-U. Ro, *Environ. Sci. Technol.*, 2011, **45**, 6275–6282.

17 J. V. Coe, J. M. Heer, S. Teeters-Kennedy, H. Tian and K. R. Rodriguez, *Annu. Rev. Phys. Chem.*, 2008, **59**, 179–202.

18 J. Heer, L. Corwin, K. Cilwa, M. A. Malone and J. V. Coe, *J. Phys. Chem. C*, 2010, **114**, 520–525.

19 M. A. Malone, S. Prakash, J. M. Heer, L. D. Corwin, K. E. Cilwa and J. V. Coe, *J. Chem. Phys.*, 2010, **133**, 185101–185107.

20 H. C. van de Hulst, *Light Scattering by Small Particles*, Dover, New York, 1981.

21 C. F. Bohren and D. R. Huffman, *Absorption and Scattering of Light by Small Particles*, Wiley-VCH Verlag GmbH, 2007.

22 A. Beer, *Ann. Phys. Chem.*, 1852, **86**, 77–88.

23 J. H. Lambert, in *Augusta Vindelicorum*, ed. E. Klett, Germany, 1760, p. 391.

24 B. Mohlenhoff, M. Romeo, M. Diem and B. R. Wood, *Biophys. J.*, 2005, **88**, 3635.

25 K. Yee, *IEEE Trans. Antennas Propag.*, 1966, **14**, 307.

26 P. K. Hudson, E. R. Gibson, M. A. Young, P. D. Kleiber and V. H. Grassian, *J. Geophys. Res.: Atmos.*, 2008, **113**, D01201.

27 A. G. Marshall and D. C. Roe, *Anal. Chem.*, 1978, **50**, 756–763.

28 M. A. Malone, Jr., *The Ohio State University*, PhD dissertation, 2012.

29 F. J. Garcia-Vidal, L. Martin-Moreno, T. W. Ebbesen and L. Kuipers, *Rev. Mod. Phys.*, 2010, **82**, 729–787.

30 J. Bravo-Abad, L. Martin-Moreno, F. J. Garcia-Vidal, E. Hendry and J. G. Rivas, *Phys. Rev. B: Condens. Matter Mater. Phys.*, 2007, **76**, 241102–241105.

31 T. W. Ebbesen, H. J. Lezec, H. F. Ghaemi, T. Thio and P. A. Wolff, *Nature*, 1998, **391**, 667–669.

32 J. Etou, D. Ino, D. Furukawa, K. Watanabe, I. F. Nakai and Y. Matsumoto, *Phys. Chem. Chem. Phys.*, 2011, **13**, 5817–5823.

33 M. L. Bell, K. Ebisu, R. D. Peng, J. M. Samet and F. Dominici, *Am. J. Respir. Crit. Care Med.*, 2009, **179**, 1115–1120.

34 F. Dominici, A. McDermott, S. L. Zeger and J. M. Samet, *Environ. Health Perspect.*, 2003, **111**, 39–43.

35 R. D. Peng, H. H. Chang, M. L. Bell, A. McDermott, S. L. Zeger, J. M. Samet and F. Dominici, *JAMA, J. Am. Med. Assoc.*, 2008, **299**, 2172–2179.

36 P. Eastwood, *Particulate emissions from vehicles by Peter Eastwood*, John Wiley & Sons, Chichester, England, Hoboken, NJ, 2008.

37 H. Hobert, *Vib. Spectrosc.*, 1995, **9**, 169–179.

38 B. T. Mossman and A. Churg, *Am. J. Respir. Crit. Care Med.*, 1998, **157**, 1666–1680.

39 C. M. Zicovich-Wilson, F. Pascale, C. Roetti, V. R. Saunders, R. Orlando and R. Dovesi, *J. Comput. Chem.*, 2004, **25**, 1873–1881.

40 W. G. Spitzer and D. A. Kleinman, *Phys. Rev.*, 1961, **121**, 1324.

41 D. A. G. Bruggeman, *Ann. Phys.*, 1935, **24**, 636–664.

42 D. Stroud, *Superlattices Microstruct.*, 1998, **23**, 567–573.

43 K. Kneipp, H. Kneipp, R. Manoharan, E. B. Hanlon, I. Itzkan, R. R. Dasari and M. S. Feld, *Appl. Spectrosc.*, 1998, **52**, 1493–1497.

44 K. Kneipp, Y. Wang, H. Kneipp, L. T. Perelman, I. Itzkan, R. R. Dasari and M. S. Feld, *Phys. Rev. Lett.*, 1997, **78**, 1667–1670.